ARMA 18–1114

SAND2018-5046C

Coupled multiphase flow and geomechanical modeling of injection-induced seismicity on the basement fault

Chang, K.W. and Yoon, H.

Geomechanics Department, Sandia National Laboratories, Albuquerque, NM, USA

Martinez, M.J.

Engineering Sciences Center, Sandia National Laboratories, Albuquerque, NM, USA

Newell, P.

Department of Mechanical Engineering, The University of Utah, UT, USA

ABSTRACT: The fluid injection into deep geological formations altar the states of pore pressure and stress on the faults, potentially causing earthquakes. In the multiphase flow system, the interaction between fluid flow and mechanical deformation in porous media is critical to determine the spatio-temporal distribution of pore pressure and stress. The contrast of fluid and rock properties between different structures produces the changes in pressure gradients and subsequently stress fields. Assuming two-phase fluid flow (gas-water system), we simulate the two-dimensional reservoir including a basement fault, in which injection-induced pressure encounters the fault directly given injection scenarios. The single-phase flow model with the same setting is also conducted to evaluate the multiphase flow effects on mechanical response of the fault to gas injection. A series of sensitivity tests are performed by varying the fault permeability. The presence of gaseous phase reduces the pressure buildup within the gas-saturated region, causing less Coulomb stress change. The low-permeability fault prevent diffusion initially as observed in the single-phase flow system. Once gaseous phase approaches, the fault acts as a capillary barrier that causes increases in pressure within the fault zone, potentially inducing earthquakes even without direct diffusion.

1. INTRODUCTION

Injection of fluid into the surface can alter the stress state, potentially inducing earthquakes driven by the failure of the critically stressed faults. The successful storage of carbon dioxide (CO_2) at commercial–scale requires to evaluate potentials of the seismic hazard and its affects on mechanical stability of the target formation (Verdon, 2013). Due to the limitation of seismic data from large-scale CO_2 storage projects, findings from other injection operations (e.g. wastewater disposal, geothermal hydrocarbon exploration) can be applied to understand the physical mechanism of induced earthquakes. However, the injection of CO_2 into brine aquifers generates the multiphase system where injected CO_2 (supercritical state) is more compressible and less dense than pre-existing brine at typical pressure and temperature of the reservoir. The difference of fluid properties may cause variations in the patterns of seismicity.

Injection-induced seismicity involves the mechanical stability of the pre-existing critically stressed fault. Direct diffusion of pore pressure into the fault changes the effective stress, potentially causing the fault failure (Zhang et al., 2013, Kerenan et al., 2014). Indirect stress transmission also deforms the fault (called as "poroelastic stressing") which can induce earthquakes without direct pore-pressure diffusion (Chang and Segall, 2016, Chang et al., 2018).

The objective of this work is to understand the multiphase flow effects on injection-induced seismicity along the fault. The perturbations in pore pressure with variation in the fault permeability are examined from the comparative study of two- and single-phase flow systems. From the numerical results, we describe the physical mechanism of potential earthquakes on the fault in the multiphase flow system.

2. MODEL DESCRIPTION

2.1. *Governing equations*

In this study, we model two-phase fluid flow (gas and water) in a porous media. The dynamics of two-phase flow in a capillary porous medium is governed by the following equations (*Peaceman*, 1977):

$$\frac{\partial(\rho_w \phi S_w)}{\partial t} = \nabla \cdot \left[\rho_w \frac{k k_{rw}}{\mu_w}(\nabla p_w - \rho_w g)\right] + Q_w \qquad (1)$$

$$\frac{\partial(\rho_g \phi S_g)}{\partial t} = \nabla \cdot \left[\rho_g \frac{k k_{rg}}{\mu_g}(\nabla p_w + \nabla p_c - \rho_g g)\right] + Q_g \qquad (2)$$

Sandia National Laboratories is a multimission laboratory managed and operated by National Technology & Engineering Solutions of Sandia, LLC, a wholly owned subsidiary of Honeywell International Inc., for the U.S. Department of Energy's National Nuclear Security Administration under contract DE-NA0003525.

which represent mass conservation of water (subscript *w*, wetting phase) and gaseous CO_2 (subscript *g*, non-wetting phase), respectively. In these equations, ϕ is porosity, ρ_α is phase density ($\alpha = w$ or g), S_α is phase (fluid) saturation, k is the intrinsic permeability, μ_α is phase viscosity, g is gravity, and Q_α denotes mass sources, either external sources or inter-phase mass transfer between fluid phases. We have also incorporated the Darcy flux terms (the terms in parenthesis on the right-hand-side), including pressure and gravitational forces, with the saturation dependent relative permeabilities, $k_{r\alpha}$ as well as capillary pressure $p_c = p_g - p_w$ defined by the van Genuchten function (van Genuchten, 1980):

$$p_c = p_{ct}[(S_w^*)^{-1/m} - 1]^{(1-m)} \quad (3)$$

$$S_w^* = \frac{S_w - S_{wr}}{1 - S_{wr} - S_{gr}} \quad (4)$$

where p_{ct} is the entry capillary pressure, n is the pore size distribution index ($m = 1 - 1/n$) and S_w^* is the normalized wetting phase saturation. $S_{\alpha r}$ is the residual saturation of each phase. The corresponding relative permeabilities are given by

$$k_{rw} = (S_w^*)^n \left[1 - \left(1 - S_w^{*\,1/m}\right)^m\right]^2 \quad (4)$$

$$k_{rg} = (1 - S_w^*)^n \left[1 - (S_w^*)^{1/m}\right]^{2m} \quad (5)$$

The pore space is assumed saturated with fluids, $S_w + S_g = 1$. The parameters for fluid properties are given in Table 1.

Table 1. Model parameters: fluid properties

	Water (w)	CO_2 (g)
ρ_α [kg/m^3]	1000	479
μ_α [Pa·s]	4×10^{-4}	3.95×10^{-5}
$S_{\alpha r}$	0.01	0
n	5	
m	0.8	
p_{ct} [Pa]	1×10^{6}	
c_f [Pa^{-1}]	4×10^{-10}	

2.2. Model domain

We model the two-dimensional (2-D) domain that represents the aerial view of the reservoir intersected by a basement fault (Figure 1). Supercritical CO_2 is uniformly injected into the center of the water-saturated reservoir (x_1, x_2) = (0,0) at the constant mass rate of 0.1 [kg/s] for 10 years. Initially the domain is at constant pressure (p_0 = 10 [MPa]) and fully saturated with water phase (S_w = 1). All boundaries have constant pressure ($p = p_0$) and water phase saturation ($S_w = 1 - S_{gr}$) conditions.

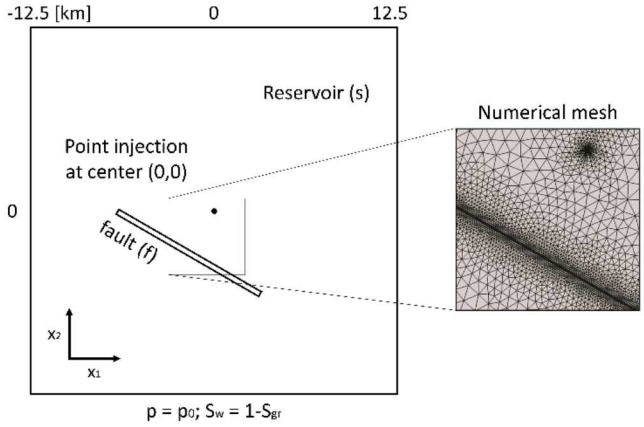

Fig. 1. Schematic description of the model domain. Refined numerical mesh is applied at the injection point and the fault zone to resolve strong gradients.

A single conductive fault located at 0.3 km away from the domain center is considered for the reference model. For the comparative study, the fault permeability (k_f) varies from 1×10^{-12} to 1×10^{-21} m^2 based on the field and laboratory measurement (IEAGHG, 2016). All parameter and their values for the reservoir and fault are listed in Table 2.

Table 2. Model properties: rock properties

	Reservoir	Fault
k [m^2]	5×10^{-14}	1×10^{-12}, 1×10^{-21}
ϕ [−]	0.25	0.02
Geometry [km]	12.5×12.5	1 (L_f)×0.005 (w_f)
f	0.6	0.75

The governing equations (1) and (2) are numerically solved with initial and boundary conditions to study the perturbation in pore pressure driven by fluid injection. The finite-element analysis is performed using COMSOL Multiphysics 5.3 (COMSOL Multiphysics, 2017), triangular elements are used for spatial discretization [Hughes, 2000], and a variable step method is employed for time integration (Dreij et al., 2011). As shown in Figure 1, mesh was highly refined near the boundaries of the faults and the injection point to resolve the strong pressure gradients.

2.3. Coulomb stress changes

The mechanical stability of the faults is effectively quantified by the Coulomb stress changes, defined in terms of the changes in stresses and pore pressure:

$$\Delta\tau = \Delta\tau_s + f\Delta\sigma_n + f\Delta p \quad (6)$$

where $\Delta\tau_s$, $\Delta\sigma_n$, and Δp are the changes in shear and normal stresses, and pore pressure respectively from the

initial state, and f is the friction coefficient. The positive values of each term imply that the fault failure is initiated under the critically stressed condition. Note that the first two terms evaluates the effect of mechanical deformation driven by the poroelastic coupling process (Chang and Segall, 2016). Without considering poroelasticity, the Eq. (6) is a function of the pore pressure change only ($\Delta\tau = f\Delta p$). Thus, the positive pressure perturbation ($+\Delta p$) implies the initiation of the mechanical instability, potentially inducing earthquakes on the fault.

3. NUMERICAL RESULTS

The change in pore pressure plays a critical role in determining the fault stability associated with CO_2 injection. We model the single-phase flow model by injection water at the same mass rate to look into the multiphase flow effect (other parameters remain the same).

Figure 2 shows the temporal distribution of pore pressure at the fault center with variations in the fault permeability for two- and single-phase flow system.

For the high-permeability fault (dash lines), immediate increases in pore pressure are observed for both two- and single-phase system. The presence of CO_2 reduces the upper limit of pore-pressure increases due to its larger mobility. Note that the magnitude of the pressure increase depends on the injection operation (rate and period) and fault properties (geometry and hydraulic characteristics).

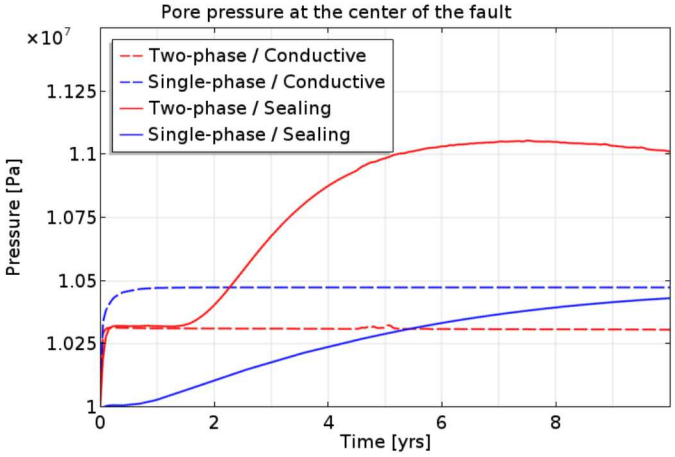

Fig. 2. Comparison of the temporal evolution of pore pressure at the center of the conductive and sealing faults (dashed and solid lines respectively) from two- and single-phase flow system (red and blue lines respectively)

For the low-permeability fault (solid lines), the pressure buildup takes more time for single-phase system because lower conductivity of the fault zone retards the pressure diffusion into it. For two-phase system, however, rapid increase in pore pressure is observed due to capillary barriers formed by the large contrast in permeability across the interface between reservoir and fault.

Figure 3 shows the spatial distribution of pore pressure at the end of injection ($t = 30$ days). In general, the CO_2-saturated region experiences less pressure buildup. Near the injection point, the pressure buildup within CO2-saturated region is up to 0.5 MPa less than one from single-phase system at given conditions.

For the high-permeability fault (top figure), pore pressure diffuses rapidly across the interface and spreads throughout the fault zone, which brings the equilibrium state of the pressure field across the interface between the fault and neighboring reservoir.

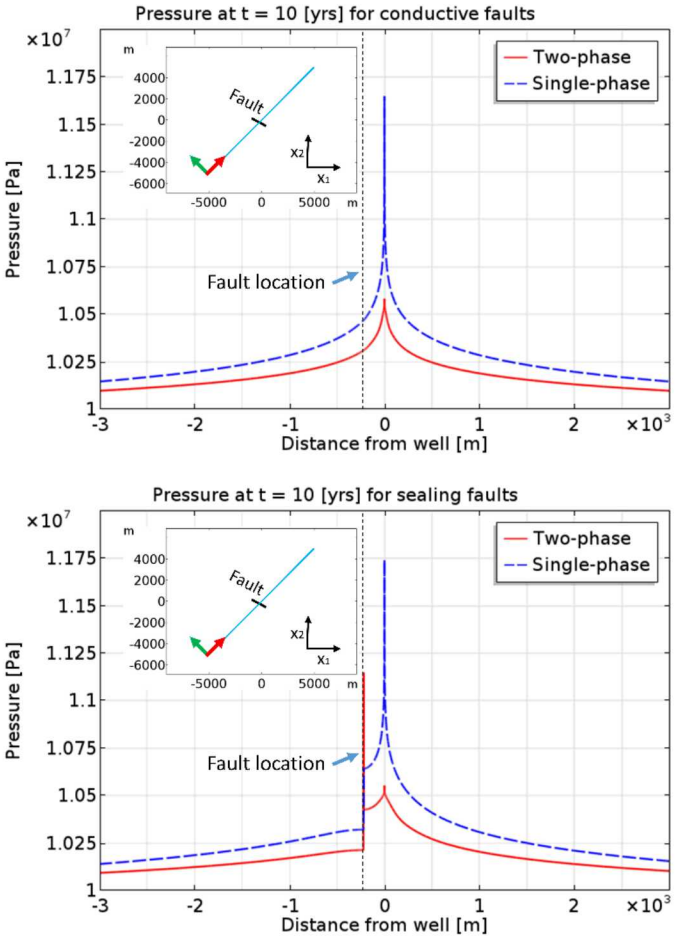

Fig. 3. Comparison of the pore-pressure distribution along the line (indicated by light blue at the sub-plot) for the conductive and sealing faults (top and bottom figures respectively) at t = 10 [yrs]. The injection well is located at x = 0 [m], and the fault location is indicated by a black dash line.

For the low-permeability fault (bottom figure), diffusion is impeded by lower diffusivity of the fault zone, acting as a hydraulic barrier. For both flow systems, the pressure accumulation is observed at the right-hand side of the fault near the injector. However, once CO_2 plume encounters the low-permeability fault, the water-wet fault acts also as a capillary barrier, which increase pore pressure dramatically within the fault zone.

Figure 4 shows the spatial distribution of pore pressure at three time steps ($t = 0$, 1, and 10 years) for the low-permeability fault case.

In the single-phase system (top figure), pore-pressure diffusion is hindered by the low-permeability fault (refer to $t = 1$ years, green line), and thus, the fault zone experience little pore-pressure buildup. At later time, the fault zone reaches the equilibrium state with a neighboring reservoir on left-hand side by slow diffusion.

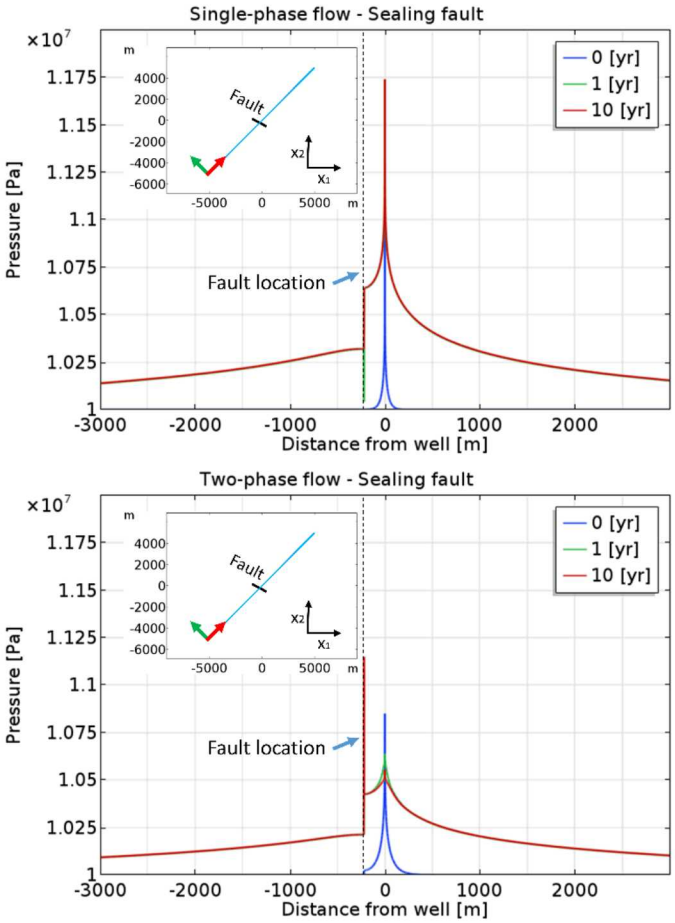

Fig. 4. Comparison of the pore-pressure distribution along the line (indicated by light blue at the sub-plot) intersecting the low-permeability fault for the single- and two-phase systems (top and bottom figures respectively) at t = 0, 1, and 10 [yrs]. The injection well is located at x = 0 [m], and the fault location is indicated by a black dash line.

In the two-phase system (bottom figure), low permeability impedes pore-pressure diffusion, which generates a quicker equilibrium state compared to ones from the single-phase system. Note that water in the low-permeability fault communicates with one in the reservoir, and thus, pressure buildup by injection increases water phase pressure within the fault as well. At later time (refer to t = 10 years, red line), the fault acts as a capillary barrier against CO_2 migration that is controlled by capillary entry pressure. Note that the volume of shale in the fault plays a significant role in determining the capillary entry pressure (experimental study showed that shale volume of greater than 40% in the fault gives p_{ct} of 55 MPa [Lyon et al., 2005]).

Larger capillary entry pressure requires pressure buildup sufficient to overcome the capillary barrier, potentially causing larger changes in $\Delta p \sim \Delta\tau$ ($\Delta p \approx 1$ MPa at given conditions). The multiphase flow effect will be one of the physical mechanisms for injection-induced seismicity on the low-permeability fault, which cannot be captured by the single-phase flow approach, in addition to the poroelastic stressing effect (Chang and Segall, 2016).

4. CONCLUSIONS

Our numerical results show that multiphase flow poses two major effects on the pressure perturbations:

- Near the injection well, larger mobility of CO_2 phase reduces pressure buildup within the CO_2-saturated zone.
- The low-permeability fault acts as a hydraulic and capillary barrier against fluid phases. Especially, the capillarity of the low-permeability fault increases water phase pressure dramatically, driven by CO_2 leak across the interface between the fault and reservoir.

Both pressure behaviors are not observed from the single-phase flow approach. These physical mechanisms in the multiphase flow systems can result in important distinction of the earthquake occurrence including their location, rate, and magnitude.

For the future study, more sensitivity test will be performed with variation in formation/fault properties and injection scenarios. Also, mechanical deformation will be included in this multiphase flow modeling, which allows the spatio-temporal changes in stresses.

ACKNOWLEDGEMENTS

This work was supported by the Laboratory Directed Research and Development program at Sandia National Laboratories. Sandia National Laboratories is a multimission laboratory managed and operated by National Technology and Engineering Solutions of Sandia, LLC., a wholly owned subsidiary of Honeywell International, Inc., for the U.S. Department of Energy's National Nuclear Security Administration under contract DE-NA-0003525. This paper describes objective technical results and analysis. Any subjective views or opinions that might be expressed in the paper do not necessarily represent the views of the U.S. Department of Energy or the United States Government. No data was used in producing this manuscript.

REFERENCES

1. Verdon, J., J.-M. Kendall, A. Stork, R. Chadwick, D. White, and R. Bissell. 2013. Comparison of

geomechanical deformation induced by megatonne-scale CO_2 storage at Sleipner, Weyburn, and In Salah, Proc. Natl. Acad. Sci., 110(30), E2762–E2771, doi:10.1073/pnas.13021561105.

2. Peaceman, D.W. 1977. Fundamentals of Numerical Reservoir Simulation, Elsevier, New York.
3. Zhang, Y., M. Person, J. Rupp, K. Elett, M. A. Celia, C. W. Gable, B. Bowen, J. Evans, L. Bandilla, P. Mozley, T. Dewers, and T. Elliot. 2013. Hydrogeologic controls on induced seismicity in crystalline basement rocks due to fluid injection into basal reservoirs, Ground Water, 51(4), 525–538, doi:10.1111/gwat.12071.
4. Kerenan, K. M., M. Weingarten, G. A. Abers, B. Bekins, and S. Ge. 2014. Sharp increase in central Oklahoma seismicity since 2008 induced by massive wastewater injection. Science 345, 448, doi:10.1126/science.1255802.
5. Lyon, P. J., P. J. Boult, R. R. Hillis, and S. D. Mildren. 2005. Sealing by shale gouge and subsequent seal breach by reactivation: A case study of the Zema Prospect, Otway Basin, in P. Boult and J. Kaldi, eds., Evaluating fault and cap rock seals: AAPG Hedberg Series, no. 2 p. 179–197.
6. Chang, K. W., and P. Segall. 2016. Injection induced seismicity on basement faults including poroelastic stressing, J. Geophys. Res. Solid Earth, 121(4), 2708–2726, doi:10.1002/2015JB012561.
7. Chang, K. W., H. Yoon, and M. J. Martinez. 2018. Seismicity rate surge on faults after shut-in: poroelastic response to fluid injection, B. Seismol. Soc. Am., accepted.
8. Van Genuchten, M.T. 1980. A closed-form equation for predicting the hydraulic conductivity of unsaturated soils. Soil Sci. Soc. Am. J., 44, 892–898.
9. COMSOL Multiphysics. 2017. COMSOL Multiphysics User's Guide. COMSOL AB, Burlington, Mass.
10. Hughes, T.J.R. 2000. The Finite Element Method Linear Static and Dynamic Finite Element Analysis, Courier Dover Publ. Mineola, NY.
11. Dreij, K., Q.A. Chaudhry, B. Jernstrom, R. Morgenstern, and M. Hanke. 2011. A method for efficient calculation of diffusion and reactions of lipophilic compounds in complex cell geometry, PLoS One, 6(8), 1–18.
12. IEAGHG. 2016. Fault permeability, 2016/13.